Article

Imaging moiré excited states with photocurrent tunnelling microscopy

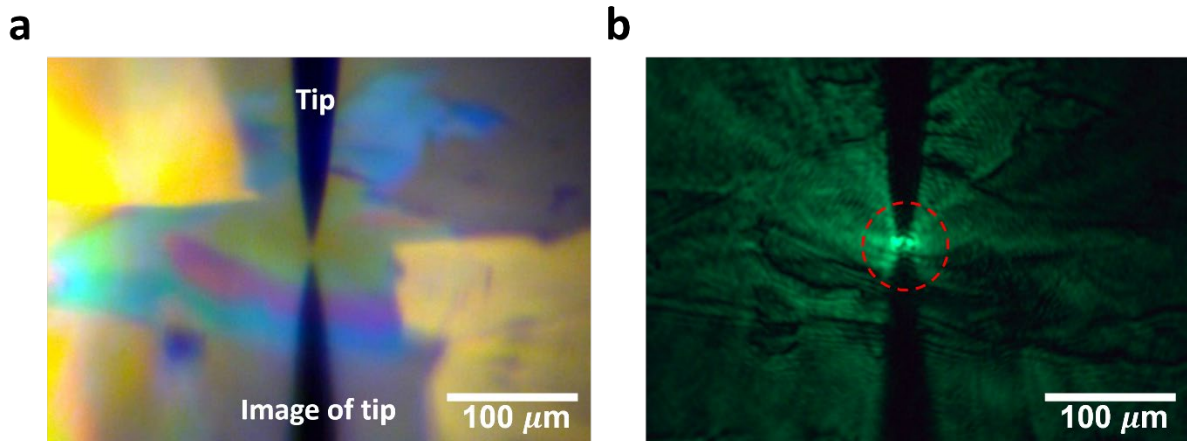In the format provided by the authors and unedited

Table of Contents

S1. Images of the laser-STM setup

a

Tip

Image of tip   100 μm

b

100 μm

Figure S1. Optical images of the tip-sample tunneling junction. a. Optical image for gated twisted WS_2 device and laser-STM setup using white light illumination. The positions of the tip and its reflected image by the substrate are labeled. **b**. Optical image of the device and setup with a 520nm continuous-wave laser focused onto the tip-sample tunneling junction. The laser spot (diameter ~10μm) is labeled with a red dashed-line circle.

S2. Extended data on the V_{bias} dependence of the ICT exciton photocurrent maps

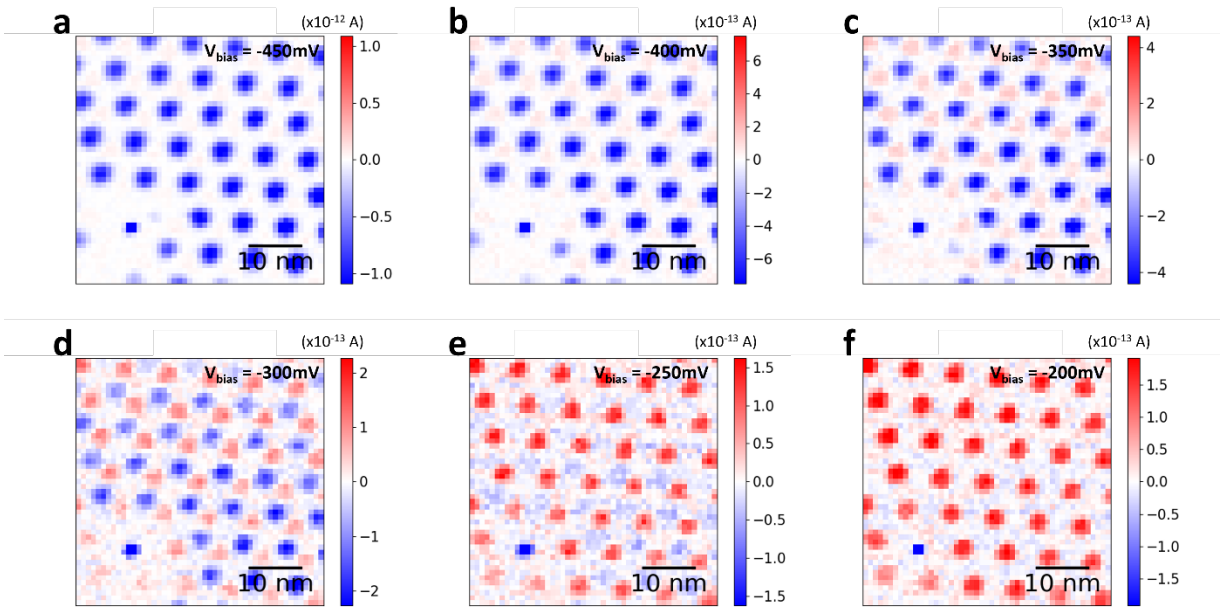Fig. S2~S4 show extended data on the V_{bias} dependent photocurrent maps of the ICT moiré excitons in t-WS$_2$ for different tip status and scanning conditions. An extra group of V_{bias} dependent photocurrent maps of the ICT moiré excitons with lower laser excitation power (P = 90uW) are shown in Fig. S13 for the purpose of studying the exciton dynamics (see more details in Section S7).
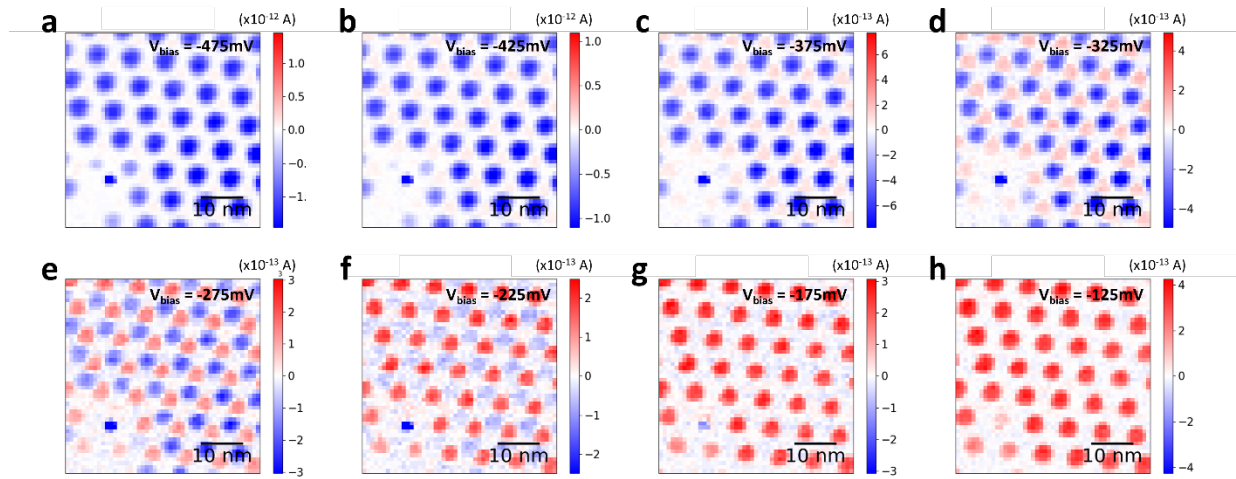
Figure S2 Extended data on the V_{bias}-dependence of the ICT exciton photocurrent maps. V_{BG} = -0.3V, V_{bias} = -3.4V, I = 11pA, h_{tip} = 200pm, and P = 900uW. STM bias offset V_0 = -275mV. V_{bias} range for coexisting positive and negative photocurrent: -375mV $\leq$ V_{bias} $\leq$ -225mV.

Figure S3 Extended data on the V_bias-dependence of the ICT exciton photocurrent maps.

V_{BG} = -0.1V, V_{bias} = -3.4V, I = 11pA, h_{tip} = 160pm, and P= 900uW. STM bias offset V_0 = -300mV. V_{bias} range for coexisting positive and negative photocurrent: -350mV ≤ V_{bias} ≤ -250mV.
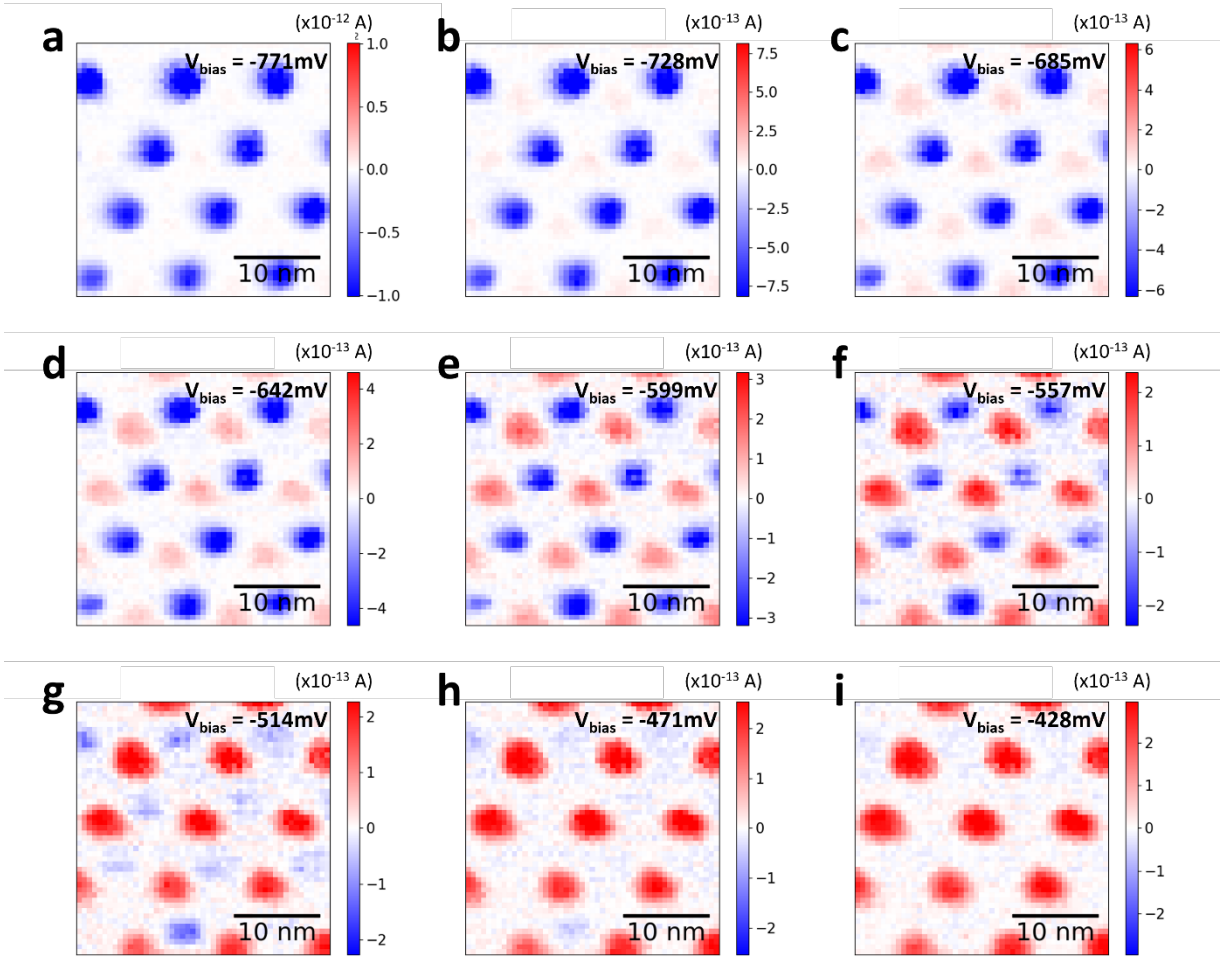
Figure S4 Extended data on the V$_{bias}$-dependence of the ICT exciton photocurrent maps.

V$_{BG}$ = 0, V$_{bias}$ = -3 V, I = 400pA, h$_{tip}$ = 0, and P= 600uW. STM bias offset V$_0$ = -599mV. V$_{bias}$ range for coexisting positive and negative photocurrent: -685mV ≤ V$_{bias}$ ≤ -471mV.

S3. Structural reconstruction of the moiré superlattice (Theory)

We modeled a moiré superlattice using two monolayers of WS_2 by applying a twist-angle of 57.72°. The monolayer unit-cell lattice constant was chosen to be 3.15 Å. The structure was constructed and relaxed using the TWISTER[1] code. The moiré unit-cell contained 3786 atoms. The structural relaxation of the moiré superlattice was performed using classical force-field calculations as implemented in the LAMMPS[2] package. The intralayer forces in the WS_2 layers were modeled using the Stillinger-Weber[3] force-field, and the interlayer interactions are included using a registry-dependent Kolmogorov-Crespi[4,5] force-field. The lowest-energy stacking configuration, AB or 2H, had the largest area in the reconstructed moiré superlattice[5–7]. The interlayer spacing between the layers was also modulated in the superlattice, with the $B^{S/S}$ stacking having the largest spacing due to steric hindrance between the S atoms of the two layers. The variation of interlayer spacing between the layers led to an inhomogeneous interlayer hybridization[6,8] in the moiré superlattice and influences the electronic structure. The reconstruction also led to a strain redistribution in the individual layers. Fig. S5 shows the interlayer spacing distribution and strain reconstruction in the 57.72° twisted bilayer WS_2. The strain was localized at the domain boundary between the AB and $B^{W/W}$ stacking[7].
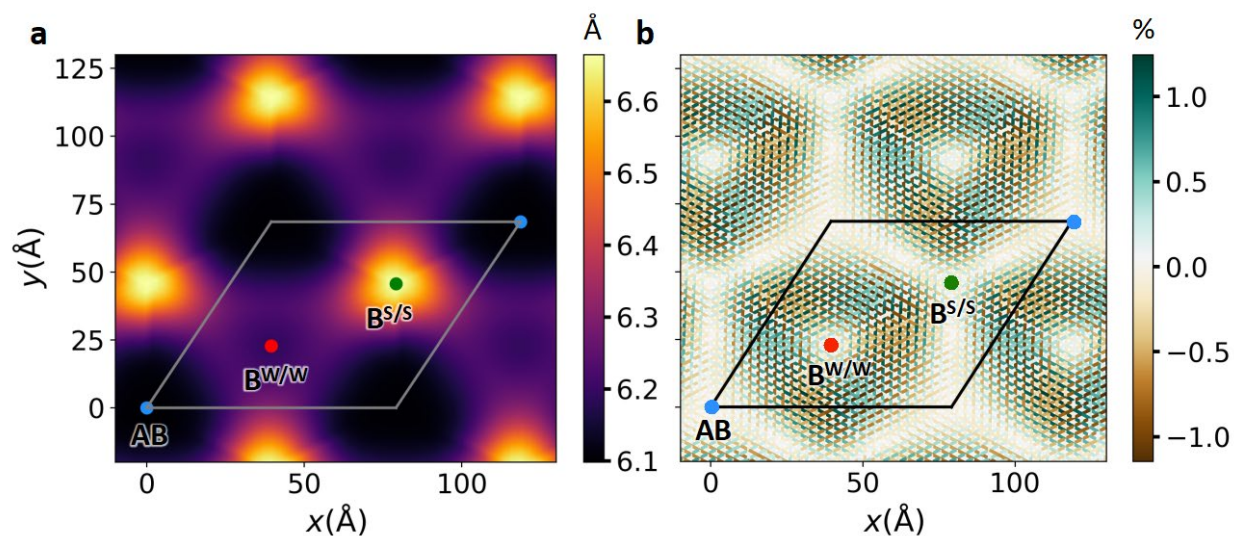
Figure S5. Theoretical structural reconstruction of the moiré superlattice. a. Distribution of the interlayer spacing (calculated as the local distance between the W atoms) in the 57.72° twisted bilayer WS_2 moiré superlattice. **b.** Strain redistribution in the bottom layer of the moiré superlattice. The strain is plotted as the percentage change in the local W-W distance from the pristine monolayer lattice constant.

S4. Electronic structure and optical calculations

The density functional theory (DFT) electronic structure calculations were carried out starting with the relaxed structure of the superlattice obtained from the force-field calculations described above. The calculations were performed using the SIESTA[9,10] code which uses localized atomic orbitals as the basis set, making it is more efficient for studying moiré unit-cells containing thousands of atoms compared to a DFT implementation using plane-wave basis sets. Relativistic optimized norm-conserving Vanderbilt (ONCV) pseudopotentials[11] used in the calculation were obtained from the PseudoDojo repository[12,13], and the exchange-correlation functional was approximated using the generalized gradient approximation[14]. Spin-orbit interaction was included in all electronic structure calculations. To capture hybridization between layers to the same level of accuracy as plane-wave basis sets, we expanded[15] the atomic basis set of the S atom to also include the 4s and 4p orbitals which have a larger spatial extent. We only sampled the zone-center γ point to obtain the self-consistent charge density. All the pristine unit-cell calculations were performed using the Quantum Espresso[16] code, which uses plane-wave basis sets. The electronic states were expanded in plane waves up to an energy cutoff of 40 Ry. We ensured that the same pseudopotential and exchange-correlation functional were used in the SIESTA and Quantum Espresso calculations. We found that the electronic states calculated using SIESTA have an overlap of over 98% with the corresponding states calculated using Quantum Espresso. We tested this for valence and conduction band edge states of pristine unit-cell AB stacked bilayer WS_2 for all the k-points in a $12 \times 12 \times 1$ sampling of the Brillouin zone (BZ).
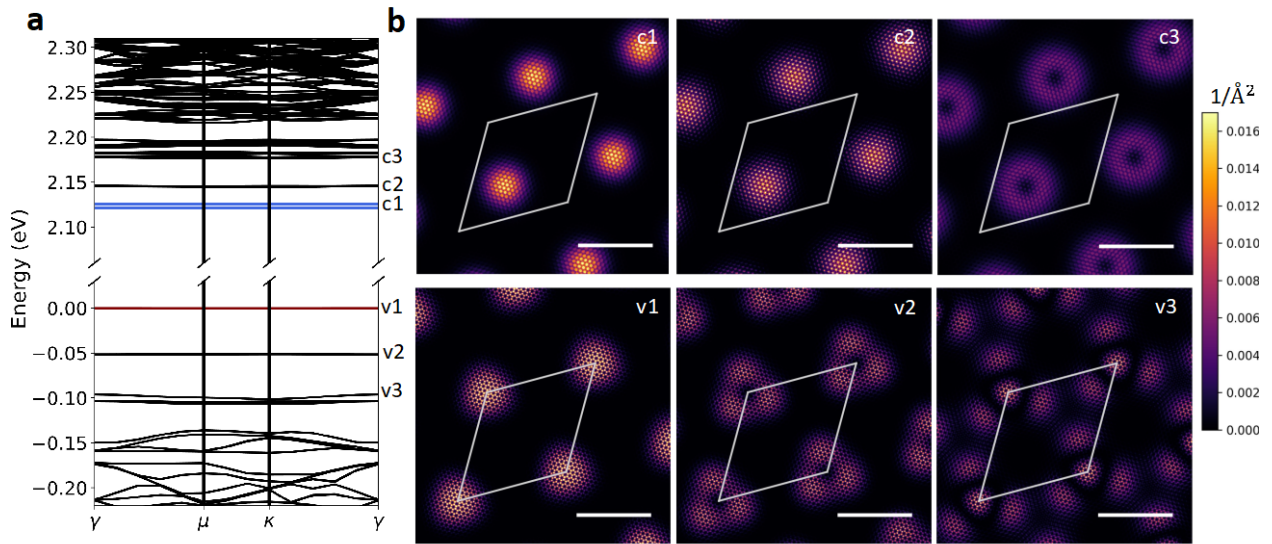
The electronic band structure and the charge density of states close to the valence and conduction band edge are plotted in Fig. S6 for the 57.72° twisted bilayer WS_2. The band gap at the DFT level is severely underestimated, while the dispersions of the bands is relatively well

captured. We computed the quasiparticle band gap for a 2H stacked bilayer by computing the electron self-energy at the GW level[17]. We used the GW correction to the $\Gamma - Q$ band gap to correct the DFT band structure of the moiré superlattice. The GW calculations were performed using the BerkeleyGW[18] package. The random phase approximation was used to compute the static dielectric matrix and screened Coulomb interaction. The plane-wave cutoff for the dielectric matrix was 30 Ry and ~6000 unoccupied states were employed. The Hybertsen-Louie generalized plasmon pole model[17] was used to extend the static dielectric to finite frequencies. The convergence of the band gap with q-point sampling was greatly improved[19] by using the recently developed nonuniform neck subsampling[20] method. The Coulomb interaction was also truncated in the out-of-plane direction[21].

Inhomogeneous interlayer hybridization and strain reconstruction leads to a deep moiré potential[7] that confines the valence band edge states to the AB site and conduction band edge states to the $B^{W/W}$ site in 57.72° twisted bilayer WS_2 (Fig. S6). The spatial distribution of the states at the valence band edge closely resembles low-energy states of a particle in an ideal triangular quantum well potential[7]. These findings are in good agreement with previous electronic structure calculations[7] on twisted bilayer MoS_2.

The electron-hole interaction kernel matrix elements of the Bethe-Salpeter equation (BSE) were computed using the BerkeleyGW package[18,22]. The pristine unit-cell matrix projection (PUMP) method (described in detail below) was used to compute the moiré superlattice kernel matrix elements as a linear combination of many pristine unit-cell kernel matrix elements. For the 57.72° twisted bilayer WS_2 we constructed the BSE effective Hamiltonian using 12 valence and 50 conduction bands with moiré BZ k-point sampling of $3 \times 3 \times 1$. We used a greater number of conduction band states than valence band states due to

the larger density of states at the conduction band edge (Fig. S6). The valence and conduction bands included in the BSE span an energy range of ~200 meV, which is larger than the binding energy of the in-plane charge transfer exciton. A static-dielectric matrix, calculated in the pristine unit-cell BZ for the AB stacking, was used to compute the pristine unit-cell kernel matrix elements. The dielectric matrix was calculated using the random phase approximation with a planewave energy cut-off of 3.5 Ry and ~400 empty states.

Figure S6. Electronic band structure and wavefunction modulation in 57.72° twisted bilayer WS₂. a. Electronic band structure of the 57.72° twisted bilayer WS_2 moiré superlattice including self-energy corrections at the *GW* level. **b.** Charge density distribution of the states at the γ point in the moiré BZ as marked in **a.** The charge density is integrated along the out-of-plane direction.

S5. Generalized pristine unit-cell matrix projection method for GW-BSE calculations

In the generalized pristine unit-cell matrix projection (PUMP) approach, we first express the twisted bilayer WS$_2$ moiré superlattice electronic wavefunctions as a linear combination of pristine wavefunctions of the individual layers. We denote the bottom pristine layer as 'a' and top layer as 'b'. The moiré valence and conduction states are constructed from the pristine wavefunctions,

$$|\psi_{v\mathbf{k}_m}^{cons}\rangle = \sum_{i=1}^{n}(a_i^{v\mathbf{k}_m}|\Phi_{a,i\mathbf{k}_m}^{val}\rangle + b_i^{v\mathbf{k}_m}|\Phi_{b,i\mathbf{k}_m}^{val}\rangle), \tag{S1}$$

$$|\psi_{c\mathbf{k}_m}^{cons}\rangle = \sum_{i=1}^{n}(a_i^{c\mathbf{k}_m}|\Phi_{a,i\mathbf{k}_m}^{cond}\rangle + b_i^{c\mathbf{k}_m}|\Phi_{b,i\mathbf{k}_m}^{cond}\rangle). \tag{S2}$$

Here, $|\Phi_{a,i\mathbf{k}_m}^{val}\rangle$ and $|\Phi_{b,i\mathbf{k}_m}^{val}\rangle$ refers to pristine superlattice valence states of layer 'a' and layer 'b', respectively, and $|\Phi_{a,i\mathbf{k}_m}^{cond}\rangle$ and $|\Phi_{b,i\mathbf{k}_m}^{cond}\rangle$ to pristine superlattice conduction states of layer 'a' and layer 'b', respectively. We have verified that the new basis sufficiently describes the original moiré electronic wavefunctions ($|\psi_{v\mathbf{k}_m}\rangle$ and $|\psi_{c\mathbf{k}_m}\rangle$) by computing the overlaps $\langle\psi_{v\mathbf{k}_m}^{cons}|\psi_{v\mathbf{k}_m}\rangle$ and $\langle\psi_{c\mathbf{k}_m}^{cons}|\psi_{c\mathbf{k}_m}\rangle$ (see Fig. S7). Using the expansion coefficients, the BSE electron-hole interaction kernel matrix elements of the moiré superlattice can be approximated as a linear combination of pristine unit-cell kernel matrix elements of layer 'a' and layer 'b',

$$\langle\psi_{v\mathbf{k}_m}\psi_{c\mathbf{k}_m}|K|\psi_{v\mathbf{k}_m'}\psi_{c\mathbf{k}_m'}\rangle$$

$$\approx \sum_{\alpha\beta\gamma\lambda=a,b}\sum_{ijpq}\alpha_i^{v\mathbf{k}_m*}\beta_j^{c\mathbf{k}_m*}\gamma_p^{v\mathbf{k}_m}\lambda_q^{c\mathbf{k}_m}\langle\Phi_{\alpha,i\mathbf{k}_m}^{val}\Phi_{\beta,j\mathbf{k}_m}^{cond}|K|\Phi_{\gamma,p\mathbf{k}_m'}^{val}\Phi_{\lambda,q\mathbf{k}_m'}^{cond}\rangle \tag{S3}$$

$$= \sum_{\alpha\beta\gamma\lambda=a,b} \sum_{ijpq} \alpha_i^{v\mathbf{k}_m *} \beta_j^{c\mathbf{k}_m *} \gamma_p^{v\mathbf{k}_m} \lambda_q^{c\mathbf{k}_m} \langle \phi_{\alpha,s\mathbf{k}_{uc}^1}^{val} \phi_{\beta,t\mathbf{k}_{uc}^2}^{cond} | K | \phi_{\gamma,y\mathbf{k}_{uc}^3}^{val} \phi_{\lambda,z\mathbf{k}_{uc}^4}^{cond} \rangle, \qquad \text{(S4)}$$

where α, β, γ and λ are layer indices, i and p are pristine valence band indices, j and q are pristine conduction band indices. The pristine states $i\mathbf{k}_m, j\mathbf{k}_m, p\mathbf{k}_m'$ and $q\mathbf{k}_m'$ in the moiré BZ are related to $s\mathbf{k}_{uc}^1, t\mathbf{k}_{uc}^2, y\mathbf{k}_{uc}^3$ and $z\mathbf{k}_{uc}^4$ in the unit-cell BZ by band folding. The kernel matrix element is in Eq. S3 refers to the pristine supercell matrix element, while the matrix element in Eq. S4 refers to the pristine unit-cell matrix element. The screened Coulomb interaction used in Eq. S4 is that of pristine AB or 2H stacking. Thus, we can express each moiré kernel matrix element as a linear combination of pristine unit-cell kernel matrix elements.

The BSE kernel[23] is given by $K = -K_d + K_x$, where K_d is a direct matrix element responsible for the attractive electron-hole interaction, and K_x is a repulsive exchange interaction. The kernel matrix elements are six-dimensional integrals,

$$\left\langle \Phi_{\alpha,i\mathbf{k}_m}^{val} \Phi_{\beta,j\mathbf{k}_m}^{cond} \middle| K^d \middle| \Phi_{\gamma,p\mathbf{k}_m'}^{val} \Phi_{\lambda,q\mathbf{k}_m'}^{cond} \right\rangle$$

$$= \int d\mathbf{r} d\mathbf{r}' \Phi_{\beta,j\mathbf{k}_m}^{cond *}(\mathbf{r}) \Phi_{\lambda,q\mathbf{k}_m'}^{cond}(\mathbf{r}) W^{AB}(\mathbf{r},\mathbf{r}') \Phi_{\alpha,i\mathbf{k}_m}^{val}(\mathbf{r}') \Phi_{\gamma,p\mathbf{k}_m'}^{val *}(\mathbf{r}'), \qquad \text{(S5)}$$

$$\left\langle \Phi_{\alpha,i\mathbf{k}_m}^{val} \Phi_{\beta,j\mathbf{k}_m}^{cond} \middle| K^x \middle| \Phi_{\gamma,p\mathbf{k}_m'}^{val} \Phi_{\lambda,q\mathbf{k}_m'}^{cond} \right\rangle$$

$$= \int d\mathbf{r} d\mathbf{r}' \Phi_{\beta,j\mathbf{k}_m}^{cond *}(\mathbf{r}) \Phi_{\alpha,i\mathbf{k}_m}^{val}(\mathbf{r}) W^{AB}(\mathbf{r},\mathbf{r}') \Phi_{\lambda,q\mathbf{k}_m'}^{cond}(\mathbf{r}') \Phi_{\gamma,p\mathbf{k}_m'}^{val *}(\mathbf{r}'). \qquad \text{(S6)}$$

The pristine kernel matrix elements that we need to compute can be classified in terms of the layer indices, α, β, γ and λ.

When all the indices refer to layer 'a' or layer 'b', the kernel matrix element is an intralayer kernel matrix element of layer 'a' or layer 'b', respectively, with a pristine AB stacking screened Coulomb interaction. For the intralayer kernel matrix elements of layer 'a', we

choose the screened Coulomb interaction with the periodicity of the layer 'a', i.e., $W_{\mathbf{q}}^{AB}(\mathbf{G}_{a}, \mathbf{G}_{a}')$

where $\mathbf{G}_{a}$ and $\mathbf{G}_{a}'$ are reciprocal lattice vectors of layer 'a'. Similarly, for the intralayer kernel

matrix elements of layer 'b' we choose the screened Coulomb interaction with layer 'b'

periodicity: $W_{\mathbf{q}}^{AB}(\mathbf{G}_{b}, \mathbf{G}_{b}')$. The choice of W has important implications for the Umklapp

processes involved. For the intralayer kernel matrix elements of layer 'a', only terms with $\mathbf{k}_{uc}^{2} -$

$\mathbf{k}_{uc}^{1} = \mathbf{k}_{uc}^{4} - \mathbf{k}_{uc}^{3} + \mathbf{G}_{a}$ are non-zero,

$$
\left\langle \Phi_{a,i\mathbf{k}_{m}}^{val} \Phi_{a,j\mathbf{k}_{m}}^{cond} | K | \Phi_{a,p\mathbf{k}_{m}'}^{val} \Phi_{a,q\mathbf{k}_{m}'}^{cond} \right\rangle
$$

$$
= \left\langle \phi_{\alpha,s\mathbf{k}_{uc}^{1}}^{val} \phi_{\beta,t\mathbf{k}_{uc}^{2}}^{cond} | K | \phi_{\gamma,y\mathbf{k}_{uc}^{3}}^{val} \phi_{\lambda,z\mathbf{k}_{uc}^{4}}^{cond} \right\rangle \delta_{\mathbf{k}_{uc}^{2}-\mathbf{k}_{uc}^{1}, \mathbf{k}_{uc}^{4}-\mathbf{k}_{uc}^{3}+\mathbf{G}_{a}} \tag{S7}
$$

The other combinations of α, β, γ and λ refer to interlayer kernel matrix elements. Since layer 'a'

and layer 'b' are separated by about 3 Å, and the wavefunctions of each layer exponentially

decay in vacuum, we only compute the dominant interlayer interactions for the direct and

exchange matrix elements. From Eq. S5, we find that the interlayer interaction is non-negligible

for the direct kernel matrix element only when $\alpha = \gamma$ and $\beta = \lambda$. For example, the contribution

of $\Phi_{\beta,j\mathbf{k}_{m}}^{cond*}(\mathbf{r})\Phi_{\lambda,q\mathbf{k}_{m}'}^{cond}(\mathbf{r})$ is small to the integral in Eq. S5 when the two conduction states are in

different layers. Similarly, the interlayer interaction is non-negligible for the exchange kernel

matrix element when $\alpha = \beta$ and $\gamma = \lambda$ (from Eq. S6). For the interlayer direct kernel

interactions, we approximate the screened Coulomb interaction to have the periodicity of layer

'a' and we further include only long-range interactions in the in-plane direction ($G_{x} = G_{x}' =$

0 and $G_{y} = G_{y}' = 0$), while fully including local-field effects in the out-of-plane direction:

$$W_{\mathbf{q}}(\mathbf{G}, \mathbf{G}') \approx W_{\mathbf{q}}(\mathbf{G}, \mathbf{G}')\delta_{G_x, G'_x=0}\delta_{G_y, G'_y=0}, \tag{S7}$$

where $\mathbf{G}$ is a reciprocal lattice vector. This approximation is valid for the interlayer matrix elements since the hole and electron are in different layers, hence the in-plane local-field effect and short-wavelength modulations of W are not as important as the long-wavelength interactions.
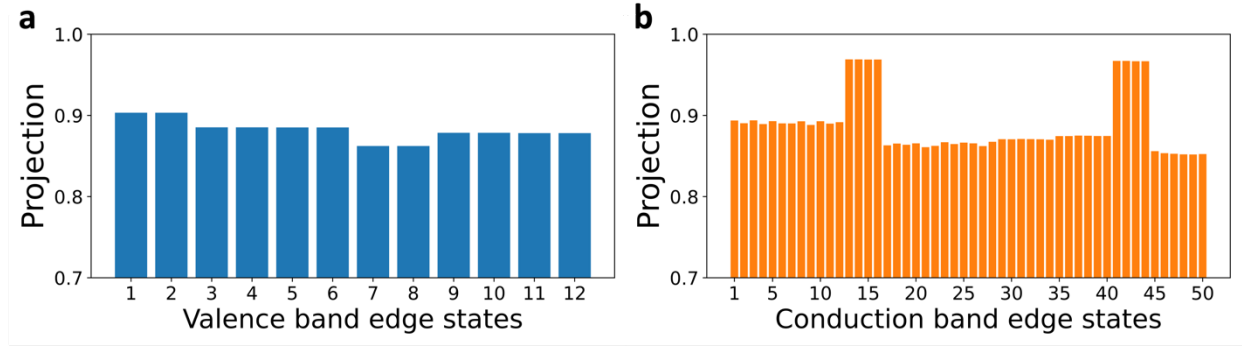
Figure S7. Projection of the constructed wavefunctions on the original wavefunctions. a. and b. Projection of the constructed 57.72° twisted bilayer WS$_2$ moiré superlattice valence ($\langle\psi^{cons}_{v\mathbf{k}_m}|\psi_{v\mathbf{k}_m}\rangle$) and conduction ($\langle\psi^{cons}_{c\mathbf{k}_m}|\psi_{c\mathbf{k}_m}\rangle$) electronic states on the original electronic states at the γ point in the moiré BZ, respectively. The moiré electronic states are constructed using a basis of 200 valence and 200 conductions states of each pristine layer ($n = 200$ in Eq. S1). The average projection is 89%. The conduction states derived from the K point in the pristine unit-cell BZ, which have less interlayer hybridization, have a higher projection compared to the states derived from the Q point.

S6. Validation of the generalized pristine unit-cell matrix projection method

We validate the approximations described in the previous section for a 38.2° twisted bilayer WS_2 for which the BSE calculations can be explicitly performed. The 38.2° twisted bilayer WS_2 contains 42 atoms in the moiré unit-cell and the structure was relaxed as described above. The electronic band structure, including spin-orbit coupling, is shown in Fig. S8. The explicit BSE was computed with a $12 \times 12 \times 1$ k-point sampling of the moiré BZ and 2 valence and 2 conduction bands. The dielectric matrix was computed in the superlattice using ~600 empty states and a plane-wave energy cutoff of 3.5 Ry. As described above, we express two valence and two conduction band edge states in the moiré superlattice as a linear combination of 8 valence and 8 conduction states of each pristine monolayer ($n = 8$ in Eqns. S1 and S2). The projection of the constructed electronic states on the original DFT computed states, $\langle \psi_{v\mathbf{k}_m}^{cons} | \psi_{v\mathbf{k}_m} \rangle$, was found to be more than 90%.

The $12 \times 12 \times 1$ k-point sampling of the superlattice BZ unfolds to a uniform $12\sqrt{7} \times 12\sqrt{7} \times 1$ k-point sampling in the pristine unit-cell BZ of each layer. The screened Coulomb interaction was computed in the pristine unit cell using this q-grid. We computed the electron-hole interaction kernel matrix elements using the generalized PUMP approach (Eq. S4) including all the approximations detailed in the above section. The absorption calculation was compared between the explicit and constructed BSE. The constructed absorption spectrum is in excellent agreement with the explicit calculation (Fig. S9), showing that our approximations are valid for a tolerance of about 10 meV in the excitation energies.
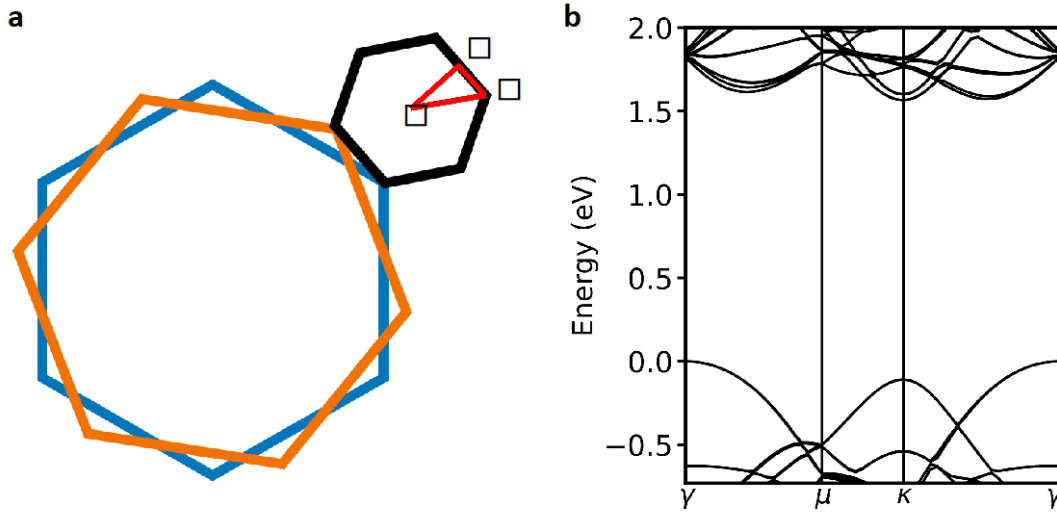
Figure S8. Brillouin zones and band structure of 38.2° twisted bilayer moiré superlattice a.
Schematic of the Brillouin zones of pristine layer 'a' (blue), pristine layer 'b' (orange) and the
38.2° twisted bilayer moiré superlattice (black) **b.** Electronic band structure of the 38.2° twisted
bilayer WS$_2$ plotted along the high-symmetry directions in the moiré BZ.
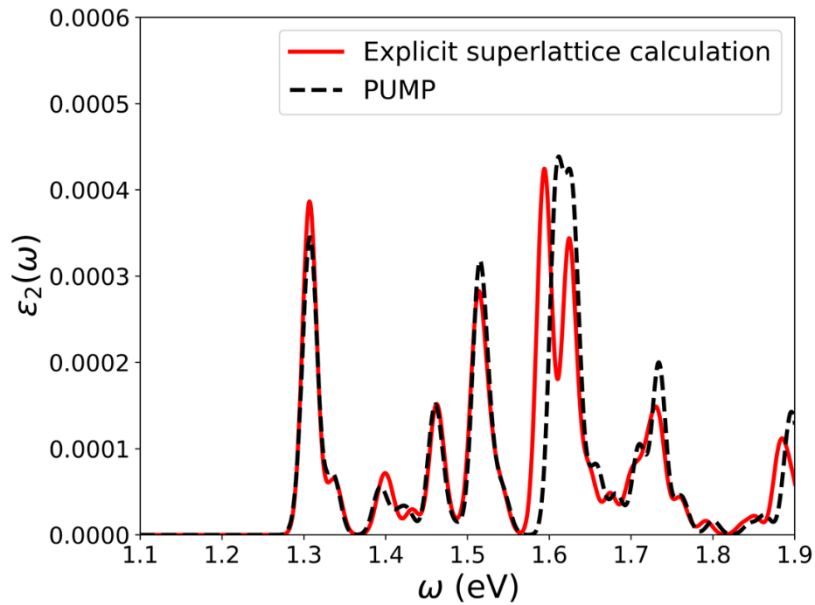
Figure S9. Validation of the generalized PUMP approach. Absorption spectrum of 38.2°

twisted bilayer WS$_2$ computed by an explicit superlattice BSE calculation compared with the

spectrum obtained using the pristine unit-cell matrix projection method.

S7. Tip-height and laser-power dependence of the tunneling photocurrent spectra

Fig. S10 shows the tunneling photocurrent spectra as a function of the tip height measured with a decreased laser power (ranging from 1000uW to 60uW) at different stacking sites (AB: Fig.S10a-e and $B^{W/W}$: Fig. S10f-j). Here the current is plotted on a log scale and the positive (orange) and negative (blue) parts use different color maps. More negative h means the tip is closer to the sample surface. To better visualize the phase space corresponding to the coexisting positive and negative tunneling photocurrent at different stacking sites ($V_{bias} \approx V_0$ as described by the scenario in Fig. 4g of the main text), we superpose the positive hole current at the AB site (extracted from Fig. S10a-e) and the negative electron current at the $B^{W/W}$ site (extracted from Fig. S10f-j) in Fig. S11. Here the positive and negative current amplitude are represented by the red and blue channels of the RGB color, respectively. Therefore, the pink region corresponds to the coexisting positive and negative tunneling photocurrent at different stacking sites. The horizontal position of the pink region, roughly corresponding to the condition $V_{bias} \approx V_0$, shows a negligible dependence on the tip height and laser power.

Fig. S12 further shows the linecut plots of the tunneling photocurrent at $V_{bias} \approx V_0$ as a function of the "nominal" tip height and laser power measured at the AB (Fig. S12a-e) and $B^{W/W}$ (Fig. S12f-j) stacking sites. A higher photocurrent is generally observed with a higher laser power. However, a quantitative analysis of the laser-power dependence of the photocurrent is challenging experimentally because the absolute tip height cannot be determined reliably across different laser powers. As described in the method section of the main text, we set the reference tip height using a closed-loop set point condition (i.e., adjusting the tip height so that the tunneling current reaches the setpoint I for a specific tip bias). The same set point condition can correspond to different absolute tip heights at different laser powers due to finite photocurrent

contribution. Since the nominal tip height is calibrated to this varying reference tip height, it is difficult to obtain a quantitative power-dependent tunneling current behavior, which requires a fixed absolute tip height.
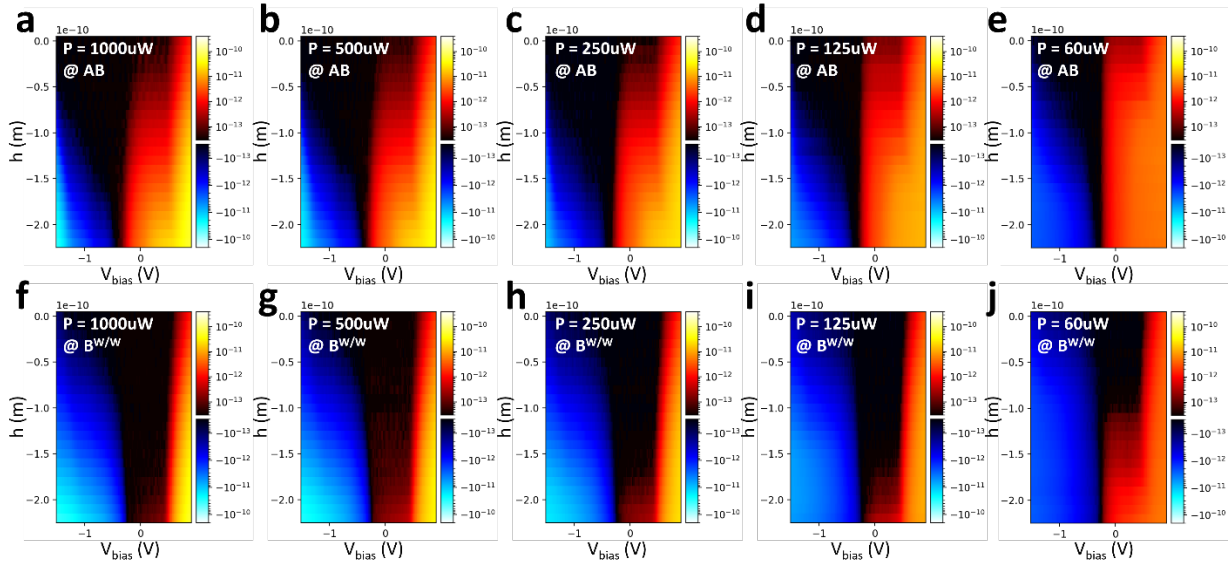
Figure S10. Tip height and laser power dependence of the tunneling photocurrent. a-j. 2D color plot of the tunneling photocurrent spectra as a function of the STM tip height (h) measured with a decreased laser power (from 1000uW to 60uW) at the (**a-e**) AB and (**f-j**) $B^{W/W}$ stacking sites. Here the current is plotted on a log scale and the positive (orange) and negative (blue) parts use different color maps. More negative values of h means the tip is closer to the sample surface. Tip height setpoint: V_{bias} = -3.5V, I = 8pA~20pA.
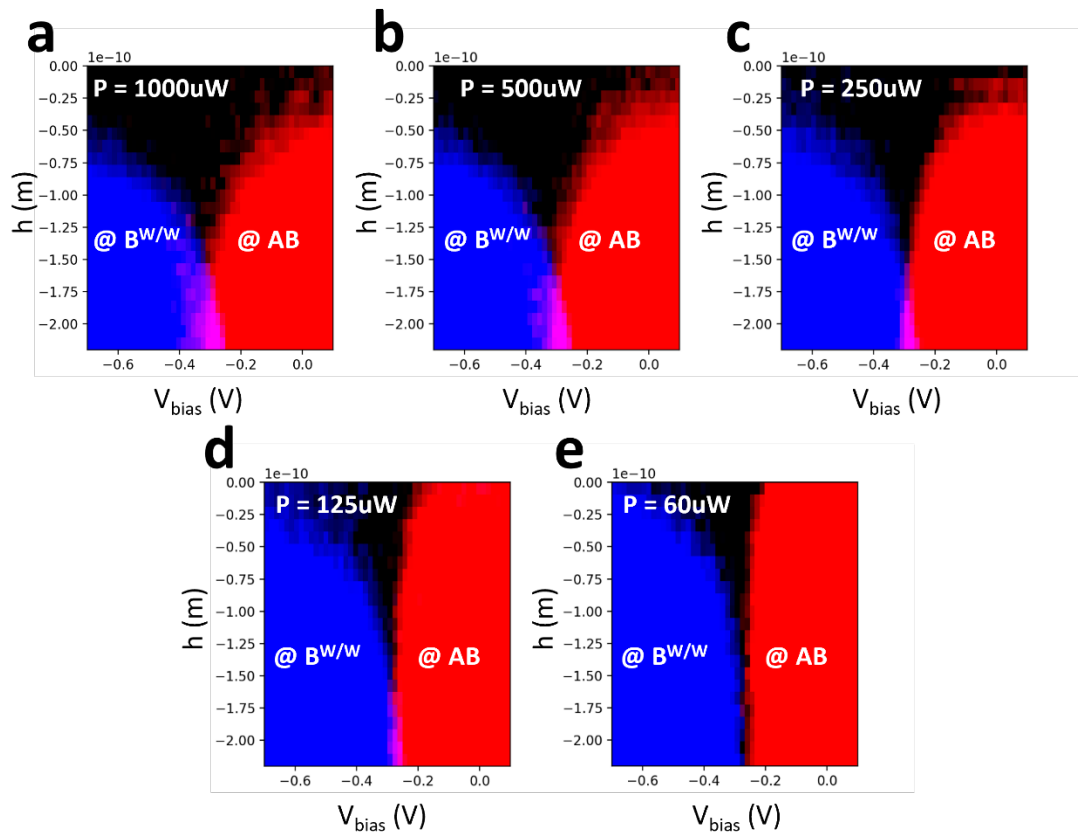
Figure S11. Comparison of the AB site hole current and $B^{W/W}$ site electron current. a-e
Superposition of the positive hole current at the AB site (extracted from Fig. S10a-e) and negative electron current at the $B^{W/W}$ site (extracted from Fig. S10f-j) with the laser power decreased from 1000uW to 60uW. Here the positive (negative) current amplitude is represented by the red (blue) channel of the RGB color intensity. The pink region in the center corresponds to the coexisting positive and negative tunneling photocurrent at different stacking sites.
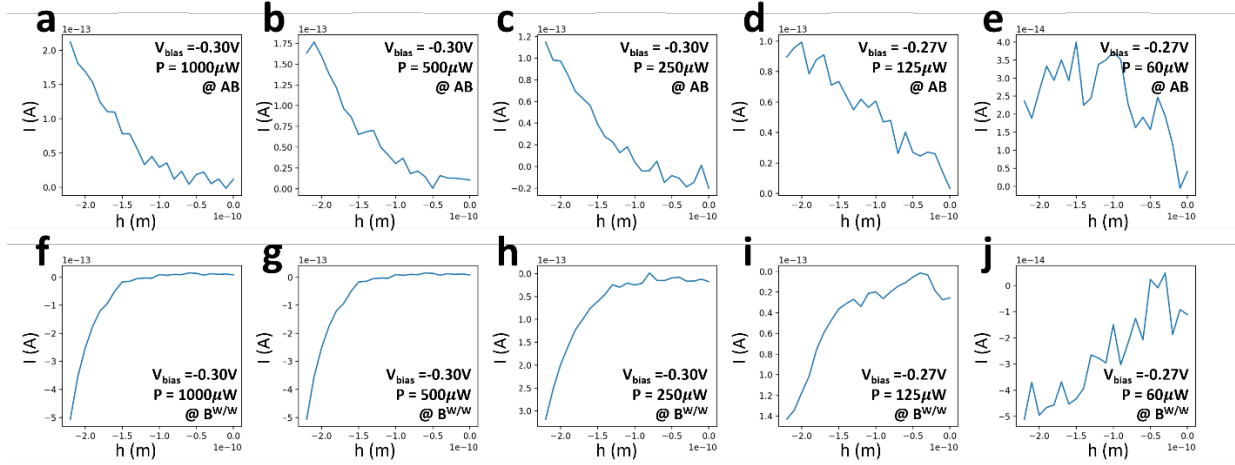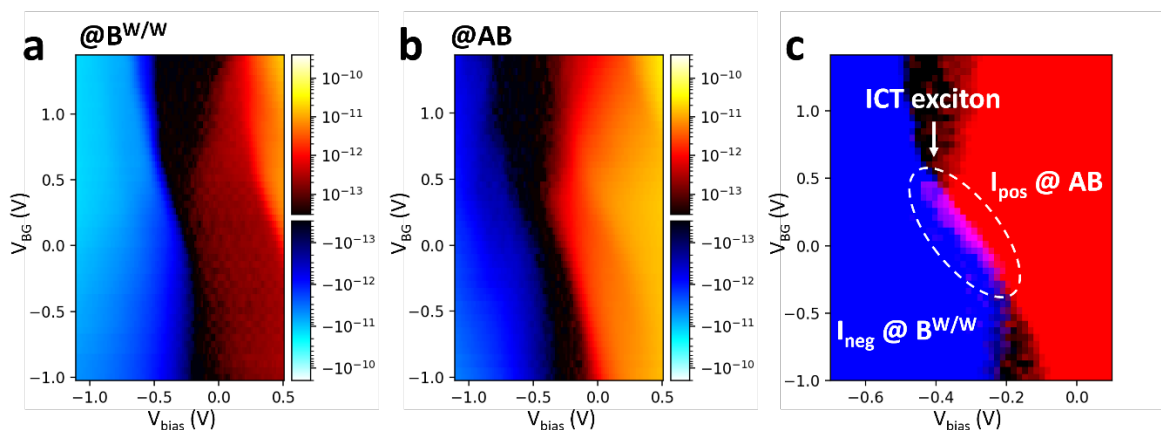
Figure S12. Tunneling photocurrent at $V_{bias} \approx V_0$. a-j. Linecut plots of the tunneling photocurrent at $V_{bias} \approx V_0$ as a function of the STM tip height (h) measured with the laser power decreased from 1000uW to 60uW at the (**a-e**) AB and (**f-j**) $B^{W/W}$ stacking sites. The values of V_0 are identified from the positions of the pink regions in Fig. S11.

S8. V_{BG} dependence of the tunneling photocurrent spectra

Fig. S13a (Fig. S13b) shows a 2D color plot of the tunneling photocurrent spectra as a function of the back gate voltage V_{BG} measured at the $B^{W/W}$ (AB) stacking site. Here the current is plotted on a log scale and the positive (orange) and negative (blue) parts use different color maps. To better visualize the phase space corresponding to the coexisting positive and negative tunneling photocurrent at different stacking sites (where the ICT moiré excitons are measured), we superpose the negative electron current at the $B^{W/W}$ site (extracted from Fig. S13a) and positive hole current at the AB site (extracted from Fig. S13b) in Fig. S13c. Similar to Fig. S11 the positive and negative current amplitude are represented by the red and blue channels of the RGB color, respectively. The pink region (marked with a dashed ellipse) exhibits a coexisting positive and negative tunneling photocurrent at different stacking sites. This corresponds to $V_{bias} \approx V_0$ under which condition the tip generate no residue electrical field and has minimum pertubation to the t-WS$_2$.

Two features are noteworthy here. (1) The $V_{bias} \approx V_0$ regime (pink region) shows a dispersive behavior. It shifts to more negative (positive) V_{bias} side with the increase (decrease) of V_{BG} around $V_{BG} \approx 0$. This is because when the t-WS$_2$ is undoped with its chemical potential in its semiconductor bandgap, tuning V_{BG} directly induces charge in the STM tip apex as the electric field can penetrate through the insulating t-WS$_2$ layer. At higher V_{BG}, more positive charge accumulates within the tip and induces a nonzero local electric field that tends to dissociate the ICT exciton. To cancel this effect, a more negative V_{bias} needs to be applied between tip and the t-WS$_2$ (effectively between the tip and the back gate graphite as the t-WS$_2$ is insulating). (2) The pink region disappears at high V_{BG}. We tentatively attribute this effect to reduced exciton lifetime when there are many doped free charge carriers at high V_{BG}. There

free carriers can interact with the excitons and decrease their lifetime through Auger process, which can lead to a much reduced tunneling photocurrent below the detection limit.

Figure S13. V_{BG} dependence of the tunneling photocurrent spectra. a,b. 2D color plot of the tunneling photocurrent spectra as a function of the back gate voltage (V_{BG}) measured at the (**a**) $B^{W/W}$ and (**b**) AB stacking sites. **c**. Superposition of the positive hole current at the AB site and negative electron current at the $B^{W/W}$ site. Here the positive (negative) current amplitude is represented by the red (blue) channel of the RGB color intensity. The pink region (marked with a dashed ellipse) in the center corresponds to the coexisting positive and negative tunneling photocurrent at different stacking sites. Tip height setpoint: V_{bias} = -3.4V, I = 20pA, h = -200pm.

References:

1. Naik, S., Naik, M. H., Maity, I. & Jain, M. Twister: Construction and structural relaxation of commensurate moiré superlattices. *Computer Physics Communications* **271**, 108184 (2022).

2. Plimpton, S. Computational limits of classical molecular dynamics simulations. *Computational Materials Science* **4**, 361–364 (1995).

3. Stillinger, F. H. & Weber, T. A. Computer simulation of local order in condensed phases of silicon. *Phys. Rev. B* **31**, 5262–5271 (1985).

4. Kolmogorov, A. N. & Crespi, V. H. Registry-dependent interlayer potential for graphitic systems. *Phys. Rev. B* **71**, 235415 (2005).

5. Naik, M. H., Maity, I., Maiti, P. K. & Jain, M. Kolmogorov–Crespi Potential For Multilayer Transition-Metal Dichalcogenides: Capturing Structural Transformations in Moiré Superlattices. *J. Phys. Chem. C* **123**, 9770–9778 (2019).

6. Naik, M. H. & Jain, M. Ultraflatbands and Shear Solitons in Moiré Patterns of Twisted Bilayer Transition Metal Dichalcogenides. *Phys. Rev. Lett.* **121**, 266401 (2018).

7. Naik, M. H., Kundu, S., Maity, I. & Jain, M. Origin and evolution of ultraflat bands in twisted bilayer transition metal dichalcogenides: Realization of triangular quantum dots. *Phys. Rev. B* **102**, 075413 (2020).

8. Naik, M. H. & Jain, M. Origin of layer dependence in band structures of two-dimensional materials. *Phys. Rev. B* **95**, 165125 (2017).

9. Soler, J. M. *et al.* The SIESTA method for *ab initio* order- *N* materials simulation. *J. Phys.: Condens. Matter* **14**, 2745–2779 (2002).

10. Cuadrado, R. & Cerdá, J. I. Fully relativistic pseudopotential formalism under an atomic orbital basis: spin–orbit splittings and magnetic anisotropies. *J. Phys.: Condens. Matter* **24**, 086005 (2012).

11. Hamann, D. R. Optimized norm-conserving Vanderbilt pseudopotentials. *Phys. Rev. B* **88**, 085117 (2013).

12. García, A., Verstraete, M. J., Pouillon, Y. & Junquera, J. The psml format and library for norm-conserving pseudopotential data curation and interoperability. *Computer Physics Communications* **227**, 51–71 (2018).

13. van Setten, M. J. *et al.* The PseudoDojo: Training and grading a 85 element optimized norm-conserving pseudopotential table. *Computer Physics Communications* **226**, 39–54 (2018).

14. Perdew, J. P., Burke, K. & Ernzerhof, M. Generalized Gradient Approximation Made Simple. *Phys. Rev. Lett.* **77**, 3865–3868 (1996).

15. García-Gil, S., García, A., Lorente, N. & Ordejón, P. Optimal strictly localized basis sets for noble metal surfaces. *Phys. Rev. B* **79**, 075441 (2009).

16. Giannozzi, P. *et al.* QUANTUM ESPRESSO: a modular and open-source software project for quantum simulations of materials. *J. Phys.: Condens. Matter* **21**, 395502 (2009).

17. Hybertsen, M. S. & Louie, S. G. Electron correlation in semiconductors and insulators: Band gaps and quasiparticle energies. *Phys. Rev. B* **34**, 5390–5413 (1986).

18. Deslippe, J. *et al.* BerkeleyGW: A massively parallel computer package for the calculation of the quasiparticle and optical properties of materials and nanostructures. *Computer Physics Communications* **183**, 1269–1289 (2012).

19. Qiu, D. Y., da Jornada, F. H. & Louie, S. G. Screening and many-body effects in two-dimensional crystals: Monolayer MoS 2. *Phys. Rev. B* **93**, 235435 (2016).

20. da Jornada, F. H., Qiu, D. Y. & Louie, S. G. Nonuniform sampling schemes of the Brillouin zone for many-electron perturbation-theory calculations in reduced dimensionality. *Phys. Rev. B* **95**, 035109 (2017).

21. Ismail-Beigi, S. Truncation of periodic image interactions for confined systems. *Phys. Rev. B* **73**, 233103 (2006).

22. Qiu, D. Y., Cao, T. & Louie, S. G. Nonanalyticity, Valley Quantum Phases, and Lightlike Exciton Dispersion in Monolayer Transition Metal Dichalcogenides: Theory and First-Principles Calculations. *Phys. Rev. Lett.* **115**, 176801 (2015).

23. Rohlfing, M. & Louie, S. G. Electron-hole excitations and optical spectra from first principles. *Phys. Rev. B* **62**, 4927–4944 (2000).